Earth Surf. Dynam. Discuss., https://doi.org/10.5194/esurf-2017-65
Manuscript under review for journal Earth Surf. Dynam.
Discussion started: 23 November 2017

Earth Surface Dynamics
Discussions
Open Access

Characterizing the complexity of seismic signals at slow-moving clay-rich debris slides: The Super-Sauze (Southeastern France) and Pechgraben (Upper Austria) case studies

Naomi Vouillamoz[1], Sabrina Rothmund[1], Manfred Joswig[1]

[1]Insitute for Geophysics, University of Stuttgart, 70174 Stuttgart, Germany

Correspondence to: Naomi Vouillamoz (naomi.vouillamoz@geophys.uni-stuttgart.de)

Abstract. Soil and debris slides are prone to rapid and dramatic reactivation. Deformation within the instability is accommodated by sliding, whereby weak seismic energies are released through material deformation. Thus, passive microseismic monitoring provides information that relate to the slope dynamics. In this study, passive seismic data acquired at Super-Sauze (Southeastern France) and Pechgraben (Upper Austria) slow-moving clay-rich debris slides ("clayey landslides") are investigated. Observations are benchmarked to previous similar case studies to provide a comprehensive and homogenized typology of seismic signals at clayey landslides. A well knowledge of the various seismic signals potentially triggered by the slope deformation is crucial for the future development of automatic detection systems to be implemented in early-warning systems. Detected seismic events range from short duration (< 2 s) quake-like signals to a wide variety of longer duration tremor-like radiations. Complex seismic velocity structures, low-quality signal onsets and non-optimal seismic network geometry severely impedes the source location procedure, thus rendering source processes characterization challenging. Therefore, we constrain sources location using the prominent waveform attenuation pattern characteristic of near (< ~50 m) seismic events. A local magnitude scale (M_L) for clayey landslides is empirically calibrated using calibration shots and hammer blows data. The derived M_L scale returns landslide seismicity rates that correlate in general with higher displacement rates. However, high temporal and spatial resolution analyses of the landslide dynamics and hydrology are required to better decipher the potential relations linking landslide-induced seismic signals to landslide deformation.

1 Introduction

Slow-moving soil and debris slides (Hungr et al., 2014) developed in tectonised marl formations are characterized by seasonal dynamics as well as by sudden (generally rainfall triggered) reactivation and liquefaction phases (e.g. Malet et al., 2005). The slow deformation of soil and debris slides is expected to generate elastic accumulation and rupture whereby seismic energy will be released within the landslide body. Therefore, passive seismic monitoring is a good approach to monitor and mitigate slope instabilities since it provides high temporal resolution data (sample rates up to 1000 Hz) in near real-time that relate to the dynamics of the landslide. The transition from steady-state sliding to a rapid transformation of the landslide in a debris flow may be detected and slope failure anticipated.

Seismic investigations of natural and artificial slope instabilities started in the 1960's with acoustic emission (AE: 10-1000 kHz) (e.g. Beard, 1961; Cadman and Goodman, 1967; Jurich and Miller Russell J., 1987) and have been complemented during the last decades by an increasing number of passive seismic monitoring studies (1-1000 Hz), carried out in various geological context. The shear boundaries of the Slumgullion earthflow in Colorado were first investigated by Gomberg et al. (1995) as a fault zone analog. The study confirmed the existence of detectable brittle deformation processes associated to the slide deformation. In Europe, investigated clayey landslides include the Heumoes slope in the Austrian Vorarlberg Alps (Walter and Joswig, 2008; Walter et al., 2011), the Super-Sauze landslide in the French Southwestern Alps (Walter and Joswig, 2009; Walter et al., 2012; Tonnellier et al., 2013; Provost et al., 2017) and the Valoria landslide in the Northern Apennines in Italy (Tonnellier et al., 2013). Case studies carried out at rockslides include for example the Randa rockslide in the Swiss Alps (Eberhardt et al., 2004; Spillmann et al., 2007); the Åknes rockslide in Norway (Roth et al., 2005; Fischer et al., 2014); the Séchilienne rockslide in the Southeastern French Alps (Helmstetter and Garambois, 2010; Lacroix and Helmstetter, 2011); and the Gradenbach, Hochmais-Atemskopf and Niedergallmigg-Matekopf deep-seated rock slope deformations in the Eastern Austrian Alps (Brückl and Mertl, 2006; Mertl and Brückl, 2007; Brückl et al., 2013).

Observed near (receiver-source distances < 0.5-1 km) seismic signals comprise microearthquake-like events, for which Gomberg et al. (1995) introduce the term 'slidequake'. Such events have been reported both at rock and debris slides and are inferred to be associated to fracture processes in the host rock, at the sliding surface, or within the landslide body. Rockfalls and avalanches signals were also characterized at steep debris slides and at rockslides (Helmstetter and Garambois, 2010; Walter et al., 2012; Tonnellier et al., 2013; Provost et al., 2017). In addition, a wide variety of tremor signals have been reported marginally (Gomberg et al., 1995; Brückl and Mertl, 2006; Mertl and Brückl, 2007; Spillmann et al., 2007; Gomberg et al., 2011; Walter et al., 2012; Tonnellier et al., 2013; Provost et al., 2017). No common typology has yet been suggested for these signals and the signal source interpretation remains speculative.

This study aims at proposing a classification of seismic signal types observed at slow-moving clay-rich debris slides ("clayey landslides") based on simple waveform and spectral attributes of the signals and using seismic observations reported by similar case studies as a benchmark. The study stresses the difficulties held in signal sources characterization: (1) Seismic velocities show drastic variations in space (highly heterogenous material) and time (change in water content and deformation of the landslide body). (2) Waveforms are strongly scattered and attenuated due to the landslide material heterogeneity and high saturation; phases onsets are difficult to identified. (3) The network geometry is in most cases non-optimal relative to the signal source. These complexities severely impact seismic event location and uncertainties of at best 20-50 m are obtained for calibration shots carried out within the recording network. The shallow installation of seismic stations in the landslide body result in high level of noise contamination of the data and the distinction between landslide-induced seismic events and other environmental (or anthropological) sources is difficult. Since the uncertainties held in the source location impact on a power-law basis the source magnitude estimation, the analysis of seismicity rate is challenging. Therefore, to reduce bias and errors in the estimation of seismicity rates, the distance attenuation function of the M_L scale was calibrated for clayey landslides using calibration shots and hammer blow datasets. Waveform attenuation patterns of natural events

Earth Surf. Dynam. Discuss., https://doi.org/10.5194/esurf-2017-65
Manuscript under review for journal Earth Surf. Dynam.
Discussion started: 23 November 2017

were then used to constrain the receiver-source distance. Using this approach, first results show an increase of seismicity rates with higher average displacement rate.

2 Data

Seismic measurements were acquired at two well-instrumented slopes: The Super-Sauze (Southwestern French Alps) and Pechgraben (Upper Austria) landslides. Both instabilities are characterized by a clay-rich matrix transporting rigid boulders of marls and limestones (including leftovers and remains of vegetation at Pechgraben) with moving rates ranging between a few mm d^{-1} up to several tenths of cm d^{-1} in the investigated areas and periods (Fig. 1a). In the monitored areas, the thickness of the instability reaches more than 10 m at Super-Sauze, but do not exceed a few meters (2-4 m) at Pechgraben. More details about the two landslides can be found in Malet (2003); Travelletti (2011); Tonnellier et al. (2013) for Super-Sauze and Lindner et al. (2014); Lindner et al. (2016) for Pechgraben.

Continuous data of three seismic campaigns are investigated (Fig. 1):

- **Super-Sauze 2010 (SZ10)**: May 28–July 24, 2010; 58 days; 18 sensors in 2 ha; average displacement of 4 mm d^{-1}.
- **Pechgraben 2015 (PG15)**: October 7-15, 2015; 9 days; 12 sensors in 6 ha; average displacement of 2 cm d^{-1}.
- **Pechgraben 2016 (PG16)**: November 8-12, 2016; 5 days; 12 sensors in 1 ha; average displacement of > 20 cm d^{-1}.

Tripartite seismic arrays were deployed with station spacing of 5-50 m. Each seismic array consists of a central three-component (3-C) short-period seismometer (Lennartz 3Dlite) which is surrounded by three to six vertical short-period seismometers (Lennartz 1Dlite). The seismometers are buried about 30 cm deep in the landslide material. Data are collected by battery powered SUMMIT M Hydra data loggers. At Super-Sauze, the array S3 consists of Noemax Agéodagis velocimeters (one 3-C and six verticals) with associated bandpass of 0.1-80 Hz, connected to a Kéhren Agéodagis acquisition system powered by solar panels. This array is part of a permanent monitoring installation (National French Landslide Observatory Facility and RESIF Datacenter, 2006). The seismometers feature therefore a robust installation and are housed in plastic drums on top of a concrete slab. A comparison of the data collected by the different installation systems proved consistent: identical waveforms featuring similar amplitudes are observed for seismic events recorded at the co-located stations S1.5, S2.6 and S3.6. At SZ10 and PG15, the seismic campaigns targeted areas of various dynamics (Fig. 1c-d). The objective was to detect potential variations in seismicity rates and test whether signals are less scattered when recorded by stations operated in stable ground. Whereas more landslide-induced signals were observed at the higher dynamic location, no significant difference was found for signals recorded by stations installed in the more stable areas. Due to the relatively large aperture (30-50 m) of the PG15 seismic arrays, many near events were recorded by less than three sensors. Consequently, a denser network configuration was designed for the PG16 campaign. Inherent difficulties of operating systems continuously on landslides resulted in incomplete datasets (Fig. 1e). This aspect must be considered in the evaluation of the seismic catalogs completeness.

3 Method

Data were analyzed following the "*Nanoseismic Monitoring*" methodology using the NanoseismicSuite software package developed at the Institute for Geophysics of the University of Stuttgart (Wust-Bloch and Joswig, 2006; Joswig, 2008; Sick et al., 2012; Vouillamoz et al., 2016). The method is supported by a realtime, analyst-guided interactive multi-parameter visualization approach. First, signals are identified by visual screening of continuous sonogram, where sonograms are logarithmically scaled spectrograms featuring a dynamic frequency-dependent noise adaptation that facilitate the detection of weak signal energies in low-SNR (signal-to-noise ratio) conditions (Joswig, 1990). The SonoView module of the NanoseismicSuite software provides a dynamic layout, where single-trace sonograms or multi-trace (array-stacked) super-sonograms are visualized on a common time line. Different resampling can be applied to the data, facilitating the focus on various event types (short/long duration, low/high frequency). Detected events are tagged and synchronized in the linked HypoLine module of the software suite for further evaluation. There, waveforms are analyzed interactively to provide an optimized graphical hypocentral solution, simultaneously processing data in network and array mode (see Joswig (2008) and Vouillamoz et al. (2016) for a comprehensive description of the HypoLine software). The strength of the method is its ability to easily detect and successfully evaluate any kind of signals without a-priori knowledge in noisy environment. The drawback is that the process is not automated. It is therefore time-consuming and not well-suited for large datasets. Results may also not be reproducible to 100 %.

Continuous sonograms of the three seismic datasets (SZ10, PG15, PG16) were screened with a focus on night time measurements to minimize false noise detections (anthropogenic noise caused by geophysicists or geotechnical work during the day). Only signals recorded coherently by three sensors at least were picked for evaluation in HypoLine. Local, regional and distant seismicity was catalogued as well. Various external sources of noise were gathered with the aim to initiate a template library of seismic signatures produced by noise events. Potential landslide-induced signals were finally classified using simple spectral and waveform features of the observed seismic signals.

3.1 Catalog design

Much attention was paid to design a consistent seismic catalog. First, all sonogram-based detection recorded consistently by at least three sensors were catalogued. Second, for each catalogued detection, waveform and spectral features of the signal were evaluated qualitatively in HypoLine and by using MATAB® routines: (1) All vertical trace seismograms of the seismic network were visualized on a common time-line with normalized and non-normalized amplitudes, using a set of pre-defined time windows (5, 10, 30, 60 and 120 s). The event duration, the signals coherency and attenuation pattern across the seismic network were checked. Traces on which the signal of interest is contaminated by noise and traces that did not record the event were tagged and discarded from further analysis. (2) For each trace that recorded the event, the spectrogram, the unfiltered waveform and a series of selected band-passed waveforms were plotted and evaluated. (3) Last, for those events featuring trackable wave packets, back azimuth and apparent velocities were calculated for individual wave packets using the interactive array processing module of the HypoLine software.

We consider the following waveform and spectral features for the classification:

- **Signal duration in seconds**. Signals are classified in three duration classes: short duration (< 2 s); medium duration (2-20 s); and long duration signals (minutes).
- **Waveform attenuation pattern**. The signals of landslide-induced seismic sources are expected to be severely attenuated. Only those events featuring prominent and consistent attenuation of the signal maximum amplitude across the seismic network are considered as potentially landslide-induced.
- **Signal onset**. Rather impulsive, broadband onsets are distinguished from emergent onsets.
- **Dominant frequency**. The distribution of the dominant energies at individual station records is evaluated in five frequency bands: 1-5; 5-20; 20-50; 50-100 and 100-200 Hz.
- **Apparent velocity of trackable wave packets**. Well-constrained apparent velocities (computed by array-processing for wave packets showing at least four traces with correlation thresholds > 70 %) range from less than 0.2 km s^{-1} to more than 5.0 km s^{-1}. We distinguish three classes of apparent velocities: < 0.5 km s^{-1} (top most volume of the landslide body); 0.5-2.0 km s^{-1} (landslide body); >2.0 km s^{-1} (sedimentary bedrock), in agreement with published velocity profiles at clayey landslides (Williams and Pratt, 1996; Tonnellier et al., 2013).

Based on these features and using previous studies as a benchmark, seismic events detected at clayey landslides are gathered in four main groups that we describe and discuss in the next section:

1. Earthquakes (local, regional and teleseismic).
2. Quakes (receiver-source distance < 50-500 m).
3. Landslide-induced tremor-like signals.
4. External sources of tremor-like radiations.

4 Unified seismic signals typology at clayey landslides

4.1 Earthquakes (local, regional and teleseismic)

Local, regional and teleseismic earthquakes are detected daily by seismic networks. Because earthquakes are potential trigger of landslides, it is important to include these events in landslides seismicity catalogs. Seismic features of earthquakes are well known from routine seismogram analysis. At clayey landslides, earthquakes produce medium to long duration signals that are recorded with similar amplitudes across the complete network. The duration and strength of an earthquake signal as well as its frequency content vary as a function of source distance and magnitude. Sharp and broadband distribution of initial frequency content is typically followed by a decrease in frequency content of the signal energy with successive phase onsets. Onsets of high-SNR events are impulsive. Individual phases with moderate scattering can be identified and return apparent velocities above 2.0 km s^{-1} (Table 1, Fig. 2).

Earth Surf. Dynam. Discuss., https://doi.org/10.5194/esurf-2017-65
Manuscript under review for journal Earth Surf. Dynam.
Discussion started: 23 November 2017

4.2 Quakes

4.2.1 Previous observations

Quake signals have been observed in previous studies carried out at clayey landslides. Gomberg et al. (1995) and Gomberg et al. (2011) report short-duration earthquake-like signals with clearly discernable, trackable wave packets that they refer as slidequakes. Dominant frequencies of slidequakes are not stated, but can be evaluated visually between 10 and 100 Hz based on the waveforms displayed in Figure 5 and Figure 6 of Gomberg et al. (2011). Walter et al. (2012) describe earthquake-like events with duration of up to 5 seconds and associated frequency content of 10-80 Hz, which they refer as slidequakes after Gomberg et al. (1995). Tonnellier et al. (2013) and Provost et al. (2017) report quake-like signals with duration of about one second, dominant frequencies around 10 Hz, emergent first arrivals and undistinguishable P- and S-waves.

4.2.2 Updated classification of quake signals

Based on duration, waveform attenuation pattern and dominant frequency content of the signals, we propose four types of quake events (Table 1; Fig. 3 and Fig. 4).

- **Type I – Near high-frequency quakes.** Signals show durations of less than 1 s and are recorded only at a few nearby stations, suggesting receiver-source distances < ~50 m (Fig. 3a). The range of signal amplitudes reaches several orders of amplitude units (Fig. 3e). Maximum amplitudes of about 10,000 nm s^{-1} were observed. High-SNR signals feature impulsive onsets. Dominant frequencies of the highest amplitude traces are in the 20-100 Hz range (Fig 4a). P- and S-phases cannot be clearly distinguished; however, successive phases may be identified based on the apparent velocity of trackable wave packets that scale within 0.2-1.8 km s^{-1} (later phases are slower).
- **Type II – Near low-frequency quakes**. Signals have duration of 1-2 s and are recorded by the complete network with amplitudes also ranging within a few orders of amplitude units and suggesting a nearby source (< ~50 m) (Fig. 3b and e). Maximum amplitudes of a few 10,000 nm s^{-1} were observed. Dominant frequencies of the highest amplitude signals stay typically in the 5-50 Hz range. The signals consist of prominent and scattered surface waves that can be tracked over the network. P- and S-phases cannot be clearly distinguished, but successive phases can eventually be discriminated based on the apparent velocity of trackable wave packets that range within 0.2-1.8 km s^{-1}.
- **Type III – Moderate distance quakes**. Signals last 1.5-2.5 s and are recorded by the complete network with consistent amplitudes across the complete network suggesting receiver-source distances of up to a few 100 m (Fig. 3c and e). Most events feature low amplitudes and are recorded just above the noise threshold (100-500 nm s^{-1}). Dominant frequencies are in the 5-50 Hz range, but weak signal energies are typically found within 50-100 Hz at the onset of the events (Fig. 4c). Apparent velocities of scattered wave packets are typically higher than 1.5 km s^{-1}. P- and S-phases are difficult to identify.

Earth Surf. Dynam. Discuss., https://doi.org/10.5194/esurf-2017-65
Manuscript under review for journal Earth Surf. Dynam.
Discussion started: 23 November 2017

- **Type IV - Local microearthquakes**. Signals have duration of 2-10 s and are recorded by the complete network with similar amplitudes (Fig. 3d-e). Successive phases can be tracked consistently over the network with apparent velocity above 2.0 km s^{-1}. Dominant frequencies are in the 5-50 Hz (Fig. 4d) but signal onsets generally display energies in the 50-100 Hz. P- and S-phases are difficult to identify.

Only type I and type II quakes are interpreted as 'slidequake' events, with the meaning they are triggered within or at the edge of the landslide body. Indeed, the short duration of the signals (< 2 s) and the prominent attenuation of the waveforms are evidence of a proximal source. The slow apparent velocities (< 2 km s^{-1}) of trackable wave packets are consistent with velocities estimated for clay-rich landslide material (Williams and Pratt, 1996; Tonnellier et al., 2013) and corroborate a source originated within the landslide body. Higher frequency content, shorter duration and few station records of type I events likely reflects a closer and maybe smaller source. Low-frequency content and longer duration of type II events may account for slower rupture velocity and maybe larger rupture area.

The high apparent velocities of trackable wave packets of type IV events as well as the moderate scattering of well distinguishable successive phases is evidence for a source origin outside of the landslide body. Whereas type IV events with duration < 3 s are likely originated very close to the landslide in the host rock, longer duration events must correspond to local (< 10 km) microearthquakes and are therefore not necessarily associated to the landslide deformation. Type III events represent likely a low-SNR boundary between type II and type IV signals.

4.3 Tremor signals

4.3.1 Previous observations

Various tremor-like signals were observed at clay-rich instabilities. Gomberg et al. (1995) and Gomberg et al. (2011) report episodes of tremor-like radiation and sinusoidal waveforms lasting tens of minutes and coherent across the network. A deeper analysis showed that many of these signals feature gliding spectral lines above 50-100 Hz in the spectrogram. Although gliding frequency tremors are known under 20 Hz at volcanoes and inferred to image change in the source properties (e.g. Hotovec et al. 2013; Unglert and Jellinek 2015; Eibl et al. 2015 and references therein), gliding harmonics are also characteristic of environmental noise signals produced by moving vehicles such as airplanes or helicopters (e.g. van Herwijnen and Schweizer 2011; Eibl et al. 2015; Eibl et al. 2017). There, the gliding harmonics correspond to the Doppler shift produced by a moving source passing a stationary receiver. At Slumgullion landslide, Gomberg et al. (2011) interpret gliding frequency tremors in the 50-100 Hz range as triggered by the action of moving vehicles along a distant (several km) road and speculate that the saturated state of the landslide may facilitate such high Q wave propagation at remote distances. However, a slide-generated source (slow rupture of faults or materials entrained within the faults like trees or boulders, or slow basal slip) is not excluded for tremor-like radiation devoid of gliding frequency and featuring the highest amplitudes at the network most remote location from the road. These events last several minutes and show dominant energies distributed broadly above 30-50 Hz and diminishing toward the Nyquist at 125 Hz (Gomberg et al., 2011).

At Super-Sauze and Valoria landslides, tremor-like signals lacking clear onsets and with undistinguishable phases were observed with duration of a few seconds to tens of seconds (Walter et al., 2012; Tonnellier et al., 2013; Provost et al., 2017). Spiky, cascading signals are interpreted as rockfalls. Such events feature repeated jolts in the 10-30 Hz that correspond to the rockfall impacts, as well as a 'noise band' in the 30-130 Hz range, likely generated by fine-grain material flows. These events are normally well recorded across the complete seismic network, with moderate waveform attenuation and maximum amplitudes reaching 1,000-10,000 nm s^{-1}. High-frequency tremor-like signals with duration of less than 20 s and maximum amplitudes under 10,000 nm s^{-1}, featuring drastic waveform attenuation and thus recorded only partially across the network were also observed (Walter et al., 2012; Tonnellier et al., 2013). Walter et al. (2012) showed that the occurrence rate of these signals correlates well with the measurements of an extensometer installed about a fissure and co-located with a 1-C seismometer at Super-Sauze, July 2009. They concluded that such signals must be triggered by fissure formations at the surface of the landslide, but also consider scratching and grinding of landslide material against (emerging) hard rock crests as potential source.

4.3.1 Updated classification of tremor signals

As in previous studies, a wide range of tremor-like signals were recorded at SZ10, PG15 and PG16. Medium duration (< 20 s) events are distinguished from long duration, minute-long lasting sequences of tremor-like radiations. While medium duration events feature trackable wave packets consisting of spikes or jolts, minute-long lasting sequences are characterized by sinusoidal waveforms and gentle rumbles, that are difficult to track coherently across the network. Due to the general waveform intricacy and the wide range of observed dominant frequency, finding an unequivocal classification for tremor events is difficult. Based on the literature and searching for consistent observations at SZ10, PG15 and PG16 we propose the following typology of tremor events, where landslide-induced tremor-like signals are distinguished from external sources of tremor-like radiations. Among the landslide-induced events, signals potentially generated by deformation and stick-slip within the landslide body are separated, when possible, from tremor-like signals originating from exogenous landslide dynamics such as rockfalls or small debris flows.

ETS-like signals (episodic tremor and slip)

ETS-like signals last a few seconds and are strongly attenuated across the network. Dominant frequency of the highest amplitude signals range within 5-50 Hz (Fig. 5 and Fig. 6a). Maximum observed amplitudes reach some 10,000 nm s^{-1}; however, most events show amplitudes no higher than a few 100-1000 nm s^{-1}. Phases cannot be identified, instead, the waveforms feature repeating and intricated spikes or jolts with prominent scattering. Individual wave packets which can be tracked return apparent velocity below 2.0 km s^{-1}.

Confirmed rockfall events

Signals generated by rockfalls resemble ETS-like signals (Fig. 5 and Fig. 6). The impacts of falling blocks produce spikes or jolts in the waveforms; loose material saltation and flow combined to the moving character of the source increase waveform intricacy. Signal duration and dominant frequency, as well as waveform attenuation pattern vary significantly depending on the size of the rockfall event and its distance to the recording network. Apparent velocities derived for individual impact signals remain below 2.0 km s^{-1}. Because rockfalls are exogenic, the signal source can eventually be caught by field observations or remote sensing. At SZ10, one ETS-like event could be matched with a single-marl block failure event caught in a high-repetition rate UAV imagery (unmanned aerial vehicle) and optical ground-based images (Rothmund et al., 2017). Since potential source areas of rockfall are known (field observable), near ETS-like signals returning back azimuth towards these areas can be classified as rockfall signals with good certainty. At Pechgraben, the low topography of the monitored area and the extremely wet and muddy conditions of the slope material during the PG15 and PG16 field campaigns preclude the occurrence of large rockfall events. However, small rockfalls consisting of landslide material failure in opening fissures (up to 20-30 cm width, 0,5-1,0 m depth) might occur and produce weak signals recorded at the nearest stations. Nevertheless, many ETS-like signals were detected across the complete network at Pechgraben, stressing the difficulty of characterizing ETS-like signal sources in the absence of additional constraints.

Harmonic tremors

Signals lasting a few seconds and consisting of harmonic peaks were observed at SZ10, PG15 and PG16 (Fig. 5 and Fig. 6c). Maximum amplitudes do not exceed a few 100-1,000 nm s^{-1}, and most signals lie barely above the noise threshold. At SZ10, harmonic tremors were observed only at single sensors. At Pechgraben, such events were detected with various waveform attenuation pattern across the seismic network, suggesting a non-unique source location origin for these signals. At PG15, harmonic tremors occur typically in minute-long lasting sequences, alternating with ETS-like signals (Fig. 4a-c). Models to explain harmonic tremors include resonance of fluid/gas driven cracks (e.g. Chouet, 1988; Schlindwein et al., 1995) as well as stick-slip (i.e. swarms of small repeating earthquakes) (e.g. Helmstetter et al., 2015; Lipovsky and Dunham, 2016). Both models could reasonably explain harmonic signals observed at clayey landslides.

Dispersive tremors

Several instances of long duration (few minutes) dispersive tremor-like signals were detected at SZ10, PG15 and PG16. Due to the dispersive character of the signals, the waveforms and spectrograms feature important variations from one station to another, rendering the events difficult to detect (Fig. 7). At the nearest stations, the signals feature high amplitude initial onset (several 10,000 nm s-^{1}). Then, the signals show prominent dispersion and waveform attenuation with increasing distance to the source. Temporal evolution of the dominant frequency content of the signals suggest a moving source. Animals can be excluded with good certainty since signals triggered by animals likely show spikier patterns, comparable to human footsteps (Fig. 8; Fig. 9). The source area of these events is difficult to access at Super-Sauze and extremely marshy at Pechgraben. No animals or animal traces could be observed there in day time. Debris flows were observed neither in the field nor in daily ground-based and UAV imagery in the affected areas. At SZ10, a secondary rotational slide was originated near the source area and crown cracks opening was observed during the detection period of the signals. Thus, we postulate rotational sliding initiation and/or opening of crown crack(s) as potential source trigger for these signals. Such a source mechanism would be compatible with field observations made in the potential source area of dispersive events at Pechgraben.

External sources of seismic noise and tremor-like radiations

Shallow installations of the seismometers in clayey materials result in important noise contamination of the seismograms, especially in the high frequency range (> 50 Hz). The variety of events produced by external source of noise is large. Signals range from short to long durations, onsets are usually emergent but sharp onsets can be found for nearby sources. In common to all signals is the absence of identifiable successive phases. Individual wave packets are difficult if not impossible to track. Maximum waveform amplitudes can be high (several 10,000-100,000 nm s^{-1}) and waveform attenuation patterns are ambiguous.

A selection of signals produced by external source of noise is presented in Figures 8 and Figure 9. Local (< 50-100 m) moving source such as geophysicists walking about the stations produce long duration spiky tremor radiations (Fig. 9b). Typical of such local moving source is the change towards higher frequency of the dominant energies of the signal as the source (the person walking) is approaching the recording station and the change towards lower frequency content of the dominant energies of the signal as the source is getting further away (Fig 8a, sonogram and spectrogram panels). Distant moving source such as airplanes and vehicles passing on nearby roads, produce long duration cigar-shaped seismograms (Fig. 8b and Fig. 9c) and spectrograms with typical gliding harmonics in the 50-200 Hz range. At PG15 and PG16, frequent timberwork and construction engines passing on the road located at the bottom of the landslide, as well as a local site effect amplifying the acoustic noise produced by airplanes in the valley resulted in important noise contamination of the data in the high frequencies. Beside anthropological noises, many environmental sources of noise were recorded but could not necessarily be distinguished in the absence of additional data at SZ10, PG15, and PG16. Wind bursts, rainfall and storms as well as water streams and bedload transports all produce long duration tremor-like radiations. These events illuminate either several frequencies or only specific ones in the spectrograms (see also Provost et al. (2017)). However, the spectrograms are clearly devoid of gliding harmonics (Fig. 8c-d). Maximum amplitudes can reach several 1,000 nm s^{-1} and waveform attenuation pattern across the network is usually incoherent (Fig. 9d).

5 Seismic source characterization

5.1 Source location

Locating seismic sources in clayey landslides is challenging: (1) The velocity structures show important variations in short distances (complex material mélange, topography) and evolves with time (slope deformation, hydrological state). Velocity models are thus only approximated by tomographic analysis for a specific time (Fig. 10a-b). (2) Scattering and attenuation of the waveforms result in low-SNR onsets and complex signal coda where phases are difficult (if not impossible) to identify. (3) The network geometry relative to the source is in most (natural) cases not optimal.

We use HypoLine (see Section 3) to analyze graphically the contribution of these parameters on the epicentral location solutions of calibration shots (SISSY, Seismic Source Impulse System, http://www.liag-hannover.de/s/s1/a1/sissy, last accessed September 13, 2017) at SZ10 (Fig. 10). Three layered velocity models simplified from Tonnellier et al. (2013)

featuring both higher and lower velocity contrasts between the landslide material and the sedimentary host rock are tested (Fig. 10a-b; Table 2). For each pair of first arrivals, the time-reversal hyperboles (hypolines) are computed at depth zero. To image the weight of phase uncertainties on the epicenter solutions, all hypolines are also computed for two shifted values of the first arrival by ± five samples (Fig. 10c). An epicenter solution is found at the highest concentration of hyperboles intersections (see Joswig (2008) and Vouillamoz et al. (2016) for details). The exercise is carried out for the three velocity models and the resulting epicenter solutions are analyzed for different station combinations. The Figure 10d shows the results obtained when using first arrivals of the three seismic arrays individually. The outcomes of this analysis can be summarized as follow:

- The applied velocity model has low impact on the epicentral solution (few meters) within the considered station network or in small distances. However, outside of the seismic network, solutions diverge significantly.
- Five samples (±) uncertainties at 1,000 Hz correspond to a high-quality phase onset pick in routine catalogs (e.g. Diehl et al., 2009). Such high-quality phase onsets derive consistent solutions within the considered station network but the solutions also diverge significantly outside of the considered seismic network.
- First arrivals of natural sources are of lower quality than those of calibration shots (Fig. 10c). Lower quality onsets have an important impact on the epicentral solutions. The domain of existence of the hypolines was tested: it shrinks for higher uncertainties and finally becomes inexistent around ± 20 samples (± 0.02 s).
- The network geometry relative to the source has the most significant influence on the location solution. Whereas the epicenter is resolved with uncertainties of about 20 m when using a set of stations surrounding the calibration shot (Fig. 10d, central panel), the potential location solutions are biased by 50 m and more when using a station network that do not surround the source (Fig. 10d, left and right panels).
- First arrivals at stations in tripartite configurations derive three zones of high-density hyperboles intersections that cannot be discriminated without additional constraints such as back azimuth information (beam-processing).
- Sources originated within the seismic network return incoherent array-processing and back azimuth data.
- Complex velocity structures and resulting waveforms scattering impedes array-processing and back azimuth information can be significantly biased. The calibration datasets at Super-Sauze and Pechgraben derive uncertainties in the order of one quadrant (± 45°) for well constrained beams (using high correlation values of four and more coherent waveform spikes).

Thus, it can be concluded that approximation in the velocity model, low-quality first arrivals and non-optimal network geometry at clayey landslides result in natural source location uncertainties ranging from tens of meters for sources originated within the network to hundreds of meters for sources originated outside of the network. Consequently, the risk of including biased data in seismicity map is high.

5.2 Waveform attenuation pattern to estimate source proximity

The drastic attenuation of waveforms within the landslide body is used to evaluate the source proximity of landslide-induced events. Distance attenuation data of calibration shots and hammer blows at Super-Sauze and Pechgraben show that signals are strongly attenuated within the first 50 m. The water content of the landslide material influences the waveform attenuation: signals are less attenuated when dryer conditions prevail (Fig. 11a). This observation is consistent with laboratory experiments (e.g. Koerner et al. 1981). The normalized difference (%) between the maximum amplitude of the signal and the median value of all maximum amplitudes for the considered event also show drastic attenuation with distance (Fig. 11b). We refer this percentage value as the scatter about the median amplitude and use it to evaluate the source distance of natural events. Thresholds values of 200 %, 1,000 % and 2,000 % are inferred to image receiver-source distances of 50 m, 20 m and 10 m from the recording station respectively. The source proximity of natural events for which the scatter about the median amplitude values remain below 200 % is considered as uncertain. Among the inferred landslide-induced events (quakes and tremors), 28 % of events at SZ10, 42 % at PG15 and 39 % at PG16 feature at least one station with a scatter about the median amplitude value above 200 %. With estimated source-receiver distance < ~50 m, these events can be reasonably assumed as originated within the landslide body or at its edges and are therefore used in the seismicity rate analysis.

5.3 Calibrating the local magnitude (M_L) scale at clayey landslides

Richter (1958) defines the local magnitude scale as Eq. (1):

$$M_L = log_{10}(A_{WA}) - log_{10}(A_0) \qquad (1)$$

where A_{WA} is originally the half of the maximum peak-to-peak amplitude in microns recorded on a Wood-Anderson (WA) seismograph and $log_{10}(A_0)$ is the distance attenuation function; i.e. a correction applied for the attenuation of the waveforms with distance. The scale is defined so that a M_L 3 earthquake writes a record of 1 mm peak amplitude on a WA seismograph at a source distance of 100 km. The distance attenuation function of the M_L scale has been calibrated empirically for many regions around the world (e.g. Bakun and Joyner, 1984; Hutton and Boore, 1987; Stange, 2006; Edwards et al., 2015); however, standard calibrated distances range within 10-1,000 km (Fig. 11a). Therefore, these distance attenuation functions are unappropriated for near recordings at landslides. Wust-Bloch and Joswig (2006) calibrated a distance attenuation function within 30-300 m for sinkhole events in the Dead Sea valley. Its slope is very similar to extrapolated distance attenuation function at distances < 1 km (Fig. 12b).

Therefore, we calibrate M_L in clayey landslides ($M_{L\text{-}LS}$) by defining the slope and the intercept of the simplest form of the distance attenuation function (Eq. (2)):

$$log_{10}(A_{0-LS}) = slope\ x\ log_{10}(D) + intercept \qquad (2)$$

where D is the receiver-source distance in km. The slope is defined using the *logfit* function (©2014, Jonathan C. Lansey), which returns regression in the form $Y = 10^{intercept} X^{slope}$ for the calibration datasets presented in Figure 11. An average slope value of -1.75 is found for the different regression curves and taken for $\log_{10}(A_{0\text{-}LS})$ (Fig. 12b).

The intercept of $\log_{10}(A_{0\text{-}LS})$ is then calculated as follow:

1. The theoretical moment magnitude M_w of a SISSY calibration shot is estimated following the Gutenberg-Richter magnitude energy relation, where $\log_{10}(E) = 1.5M_w + 11.8$, E being the radiated seismic energy in ergs. Using E = 240 Kilojoule (SISSY working principle, http://www.liag-hannover.de/en/s/s1/a1/sissy/project-presentation.html, last visited September 21, 2017), we find $M_{w\text{-}SISSY} = 0.39$.
2. Following Deichmann (2017), we derive M_L of a SISSY shot as $M_{L\text{-}SISSY} = 1.5M_{w\text{-}SISSY} = 0.58$.
3. The intercept of $\log_{10}(A_{0\text{-}LS})$ is found using $M_{L\text{-}SISSY} = 0.58$ with the mean slope of the regression curves (-1.75) and the average 0-to-peak amplitude of the calibration shots in 1 m distance (A = 5e10^6 nm s^{-1}).

The calibrated M_L in clayey landslides finally writes as Eq. (3):

$$M_{L-LS} = log_{10}(A) + 1.75 log_{10}(D) - 0.87 \tag{3}$$

where A is the maximum (vertical trace) 0-to-peak amplitude of the signal in nm s^{-1} and D the receiver-source distance in km.

The calibrated distance attenuation curves are steeper than the average slope of regional $-\log_{10}(A_0)$ curves (Fig. 12b). However, since no simple relation exist between A_{WA} in µm as used in the calculation of standard M_L and A in nm s^{-1} as read on a detection trace in landslides, the comparison of standard distance attenuation functions $\log_{10}(A_0)$ with $\log_{10}(A_{0\text{-}LS})$ is not straightforward. Well imaged in Figure 12b, is the strong influence of various water saturation of the landslide material prevailing during the different calibration measurements, which can result in bias of one order of magnitude or more at distances smaller than 100 m. The range of potential M_L of landslide-induced events is evaluated in Figure 13. $M_{L\text{-}LS}$ is plotted as a function of the amplitude read in nm s^{-1} using $\log(A_{0\text{-}LS})$ for three receiver-source distances (1, 10 and 100 m). Considering the range of observed signal amplitudes, the graphic shows that landslide-induced seismicity must scale within about $-3.0 < M_{L\text{-}LS} < 1.0$. This agrees with the potential magnitude range that can be inferred from field observations and assumptions, where active seismogenetic structures are expected to fall in the decimeter-meter range.

5.4 Seismicity catalogs at clayey landslides

Detected events were gathered into the four main groups described in Section 4 (earthquakes, near quakes, tremors, external source of tremor-like radiations). Since many events feature hybrid characteristics, the distinction between sub-classes of events was often not straightforward. For instance, we observed frequent near quakes (type I and II) featuring short duration harmonics in their coda at Pechgraben. As well, several instances of near quakes doublets, similar to short-duration ETS-like signals were observed at both landslides. A systematic template matching analysis as performed in Gomberg et al. (2011) was not carried out. Instead, we cross-correlated the waveforms of individual event classes using a 1-30 Hz bandpass filter. No events sharing high waveform similarity such as the repeating events of Gomberg et al. (2011) were found by this analysis. Because of the high uncertainties held in the source location (Section 5.1), no seismicity maps were produced. Events showing a scatter about the median amplitude above 200 % are considered to be originated in the vicinity (10, 20 or 50 m, see Section 5.2) of the highest amplitude station. Only these events are used in the magnitude catalog to avoid bias in seismicity rate estimations (Fig. 14).

5.4.1 Seismicity rates

The Figure 14 shows the temporal $M_{L\text{-}LS}$ distribution of near (< 50 m) landslide-induced seismic events relative to displacement and precipitation data. Average displacement rates at Super-Sauze 2010 were much lower than annual average values observed since 1991 (see Figure 5.25 in Travelletti, (2011)). During the SZ10 field campaign, displacement was measured daily at the reference dGNSS station (differential global navigation satellite system) located next to station S2.3. The eight-week average displacement in the study area is about 0.4 cm d^{-1}. Two main acceleration phases that unevenly follow rainfall events around June 16 and June 26, 2010 reach a maximal displacement of 1.5 and 1.9 cm d^{-1}. Near landslide-induced events show temporal clustering which do not necessarily correlate to acceleration peaks. No link is found between the energy radiated by local and regional earthquakes and landslide-induced seismicity (Fig 14b). At PG15, an average displacement of about 2 cm d^{-1} was derived on the most active part (array S1) from dGNSS data collected once a week. At PG16, the mean displacement during the campaign was estimated above 20 cm d^{-1} by triangulation, using grids of fixed nails both on the stable and active part of the slide. At both PG15 and PG16, the short durations of the field campaigns combined to the low resolution of the kinematics data prevent us to analyze precisely the potential links between landslide-induced seismicity and landslide dynamics (Fig. 14c). Landslide-induced seismic events also cluster in time at Pechgraben: events typically occur in sequences lasting a couple of minutes to hours. Seismicity rates ($M_L > -1$) for the three campaigns show a clear increase with increasing average displacement rates (Fig. 14d).

6 Conclusion and Outlook

We propose a unified typology of seismic signals observed at slow-moving clay-rich debris slides by comparing passive seismic recordings of three campaigns and using published similar case studies as a benchmark. The highly heterogenous and water-saturated state of the material within the slides result in strongly attenuated and scattered waveforms. Signals generally consists of complex and intricated surface waves, where P- and S-phases cannot be clearly distinguished and successive phase (or wave packets) onsets are difficult, if not impossible to pick. Therefore, very simple waveform and spectral attributes of the signals are used for the classification (see list in Section 3.1). The principal discriminating parameters we find to differentiate landslide-induced seismic signals from external unrelated sources are (1) the prominent waveform attenuation of near (< ~50 m) sources across the recording network (Section 5.2) and (2) the low apparent velocity (< 2 km s^{-1}) of trackable wave packets that also applies for landslide-related signals generated in 50-500 m (estimated) receiver-source distances. Two main classes of landslide-induced signals are found: (1) quake-like signals ('slidequakes') and (2) a variety of tremor signals (Sections 4.2-4.3). Because of complex seismic velocity structures, low-SNR signal onsets and non-optimal network geometry, source location uncertainties scale at best with the size of the used seismic network. Errors in estimated receiver-source distance also adversely affect event magnitude estimation. Consequently, it is difficult (and speculative) to characterize source processes and evaluate seismicity rates. Using waveform attenuation pattern to estimate receiver-source distances, we nevertheless computed M_L for near signals (< ~50 m), applying a distance attenuation function calibrated for clayey landslides. Results show an increase of seismicity rate with higher average displacement rates. Although much attention was paid to derive unbiased magnitude catalogs, uncertainties are still high. In addition, the catalogs may be incomplete in the lower magnitude range due to incomplete datasets (see Section 2). Consequently, we did not derive b-values.

Since passive seismic methods alone do not allow a detailed characterization of seismic source processes taking place at clayey landslides, it is recommended to supplement seismic data with high spatial-temporal resolution remote sensing, geodetic, geotechnical, geophysical, meteorological and hydrological measurements. One inconvenient is that ground-based measurements on the landslide during the day result in high anthropological noise level, corrupting a significant part of day-time seismic measurements, when other measurements are available. The seismic monitoring of Super-Sauze 2010 was part of a multi-disciplinary field experiment. Dynamics of the landslide could be derived from daily UAV orthomosaics, ground-based optical images and dGNSS measurements over a dense grid covering the seismic arrays (Rothmund et al., 2017). In one promising instance, a single marl-block failure event could be matched both in the imagery and the seismic datasets. Other dynamics like displacement or fissure development (opening and clogging) could also be observed. Intrinsic differences in spatial and temporal resolution of the various datasets (lower sample rate but higher spatial resolution of remote sensing, kinematics and geotechnical measurements in comparison to the instantaneous nature but high spatial uncertainty of seismic detections) generally prevent to link with certainty seismic detections to remote sensing observations. We nevertheless consider that multi-disciplinary approaches can bring key additional constraints to better understand landslide-induced seismicity.

Future directions of this study involve a detailed comparison of the various datasets at Super-Sauze. The aim will be to precisely evaluate the degree to which the main limitation of passive seismic monitoring (high spatial uncertainty of the detected seismic events and hence speculative sources characterization) can effectively be compensated by remote sensing and other geodetic and geotechnical information. Similarly, at Pechgraben, data acquired by a GB-InSAR (ground-based interferometry synthetic aperture radar) together with one seismic array during a highly active one-month period in November-December 2016 by the EOST, University of Strasbourg, France, will be analyzed and benchmarked to seismic data with the aim to improve our understanding of the mechanisms driving brittle deformation in clayey landslides.

Data and resources

The Super-Sauze and Pechgraben seismic datasets used in this study are stored at the Institute of Geophysics of the University of Stuttgart, Germany, in SEG-2 and MSEED data format. Request to these data can be addressed to the authors. Computations and plots were done with MATLAB (www. mathworks.com/products/matlab, last accessed November 10, 2017) under a campus license of the University of Stuttgart. The MATLAB spectrogram code and colormap was provided by Clément Hibert of the EOST, University of Strasbourg, France.

Acknowledgements

This work was funded by an early postdoc mobility fellowship of the SNSF (Swiss National Science Foundation, grant P2FRP2_158749). Birgit Jochum, David Ottowitz and Robert Supper of the Geological Survey of Austria in Vienna are warmly acknowledged for sharing datasets, as well as providing insightful tips and help for the field work in Pechgraben. Jon Mosar of the Institute of Earth Sciences of the University of Fribourg, Switzerland is thanked for lending seismometers and dataloggers for the Pechgraben seismic campaigns. The authors are very grateful to Clément Hibert, Jean-Philippe Malet and Floriane Provost of the EOST, Strasbourg University, France, for fruitful inputs in this project as well as for sharing datasets and codes. The authors thank Marco Walter, Ulrich Schwaderer and Patrick Blascheck of the IfG (Institute for Geophysics) of the University of Stuttgart for their support at Super-Sauze 2010 seismic monitoring campaign and their help in the seismic data pre-process. Juan-Carlos Santoyo Campus (IfG, University of Stuttgart) is warmly thanked for his participation to the 2015 Pechgraben field campaign.

Tables and Figures

Table 1. Seismic features of seismic signal types detected at slow-moving clay-rich debris slides. Features are indicated for high-SNR high-energy signals.

	Signal duration	Signal onset	Attenuation pattern	Dominant frequency	Number of recording station	Max. amplitude (order in nm s^{-1})
Earthquakes						
Local/Regional	~10-60 s	impulsive	none	1-20 Hz	all	10000
Tele	60 s-minutes	emergent	none	< 5 Hz	all	100
Quakes						
Type I Near high frequency	<1 s	impulsive	clear	20-100 Hz	< 5	1000-10000
Type II Near low frequency	1-2 s	impulsive	clear	5-50 Hz	all	1000-10000
Type III Moderate distance	~2 s	impulsive	ambiguous	5-50 Hz	all	1000
Type IV Local microearthquake	2-10 s	impulsive	ambiguous	5-50 Hz	all	1000
Tremors						
Landslide-induced tremor-like signals						
ETS-like	<20 s	emergent	clear	5-50 Hz	<5-all	1000-10000
Rockfall	5-10 s	emergent	clear	5-100 Hz	<5-all	100-10000
Harmonic	<5 s	emergent	clear	5-20 Hz	<5	100-1000
Dispersive	30-120 s	emergent	clear	50-250 Hz	<5-all	10000
External source of tremor-like radiations						
Footsteps	5 s-minutes	emergent	clear	5-100 Hz	< 5-all	10000
Gliding frequency	20 s-minutes	emergent	none	50-100 Hz	all	1000
Meteorological	20 s-minutes	emergent	ambiguous	20-250 Hz	all	10000

Table 2. Three simplified layered velocity models at clayey landslides.

Layer thickness (m)	Model 1	Model 2	Model 3
10	0.4 km s-1	0.65 km s-1	0.8 km s-1
Half-space	2.3 km s-1	1.5 km s-1	2.3 km s-1

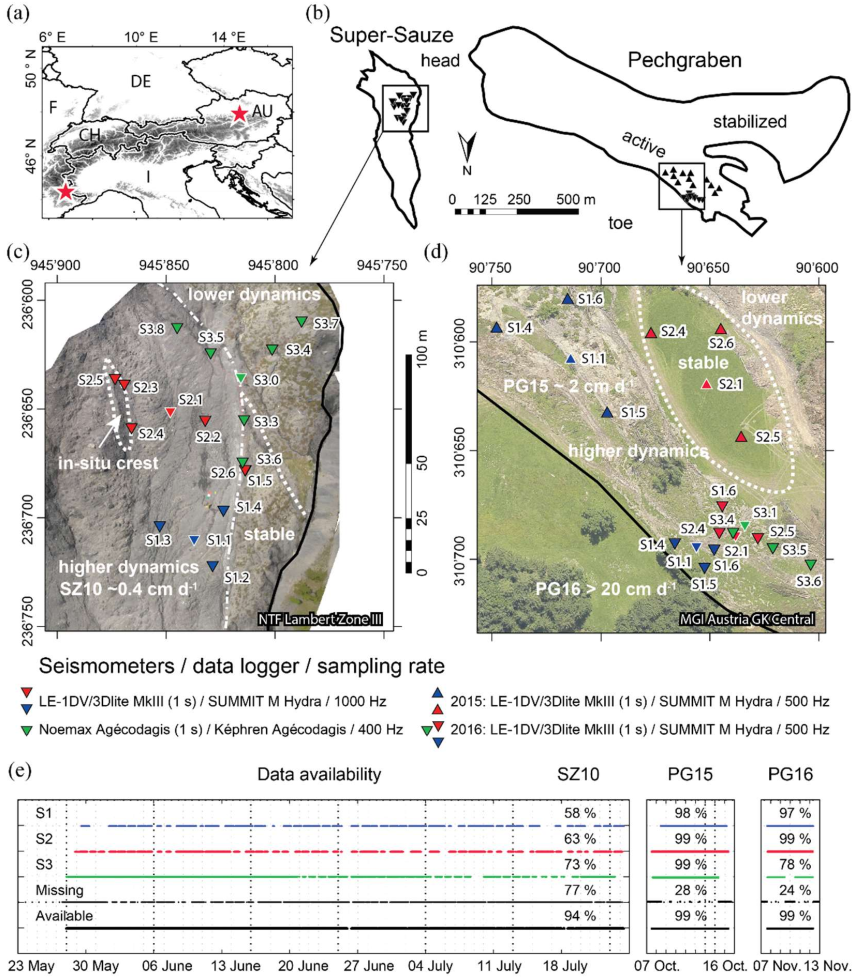

Figure 1. Data overview. (a) Location of Super-Sauze (Southeastern France) and Pechgraben (Upper Austria) clayey landslides (stars). (b) Orthogonal projection of Super-Sauze and Pechgraben instabilities with situation of instrumented areas. (c) Zoom into Super-Sauze seismic network in 2010 (SZ10). (d) Zoom into Pechgraben seismic networks deployed in 2015 (PG15) and 2016 (PG16). In (c-d), zones of higher and lower dynamics and the average displacement rates prevailing during individual field campaigns are indicated by white dotted lines. 3-C seismometers triangle symbols are highlighted by white outlines. Orthophotos credits: Super-Sauze, Rothmund et al. (2017); Pechgraben, Lindner et al. (2014); Lindner et al. (2016). (e) Data records availability for individual seismic arrays (S1, S2 and S3) based on 2 minutes data segments. The *missing* line indicates incomplete records (measurements from one or two arrays are missing); the *available* line shows where at least one array is recording.

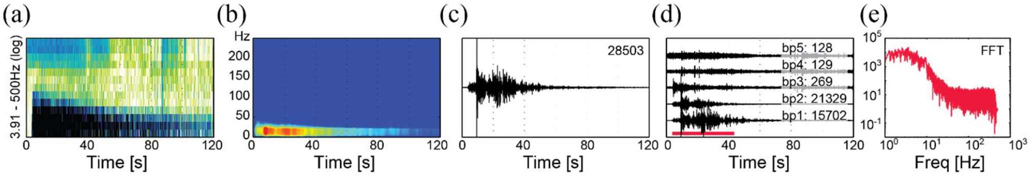

Figure 2. Seismic features of an earthquake. Regional event (in 110 km distance) of June 30, 2010 11:53 with M_L 4.3 at Saint-Jean-de-Maurienne, France, recorded at SZ10, station S2.1 at t_0 2010.06.30 11:54:00. (a) Sonogram: A typical sonogram pattern for an earthquake maximizes signal onset and enhances changes in distribution of signal energy as a function of time and frequency. (b) Spectrogram (window: signal length/30; overlap: 90 %; colormap and code provided by Clément Hibert, EOST (Ecole et Observatoire des Sciences de la Terre), University of Strasbourg, France). (c) Unfiltered seismogram. (d) Bandpass filtered seismograms (bp1: 1-5; bp2: 5-20; bp3: 20-50; bp4: 50-100; bp5: 100-200 Hz). (e) Fast Fourier Transform (FFT). This layout is applied to all figures presenting the seismic signals classification. Time indication is always UTC. Waveforms maximum 0-to-peak amplitudes are indicated in nm s^{-1} above the seismograms in (c) and (d). The signal window for which the FFT is computed is indicated by the red horizontal line in (d).

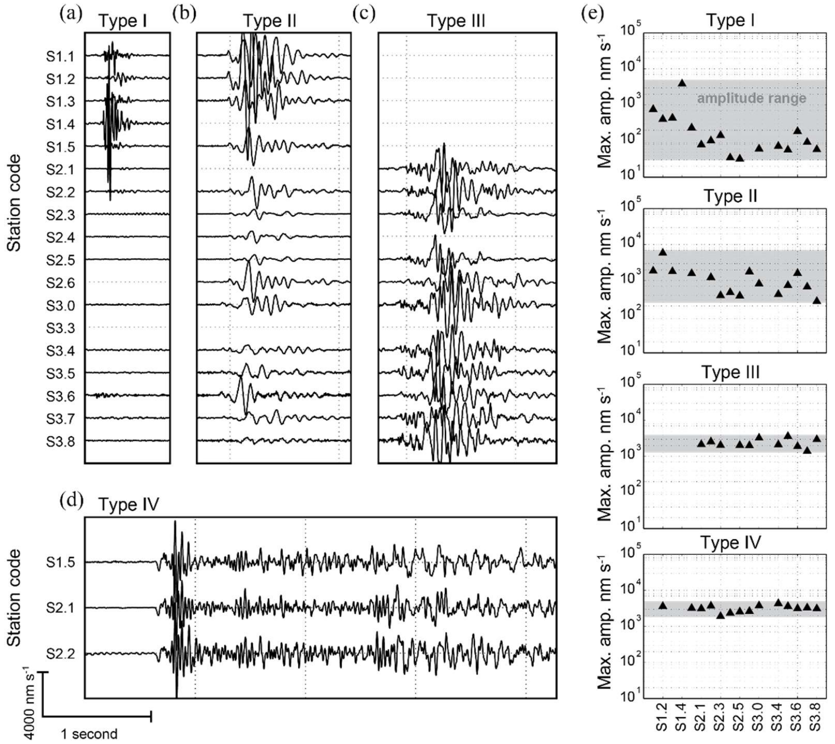

Figure 3. Vertical trace seismograms of quake events recorded at SZ10 (see station location and nomenclature in Figure 1). A fixed amplitude and time scale is applied to all waveforms (bottom left). (a) Near high frequency quake type I (May 29, 2010, 23:05:05). (b) Near low frequency quake type II (June 26, 2010, 18:44:55). (c) Moderate distance quake type III (June 17, 2010, 15:32:45). (d) Local microearthquake type IV (June 7, 2010 11:24:29). Note the highly coherent successive phases and moderate scattering. (e) Maximum amplitudes (log nm s^{-1}) recorded at individual stations for the four events displayed in a-d. Large amplitude range (grey rectangles) discriminate events types I and II from events type III and IV which typically feature narrow amplitude ranges.

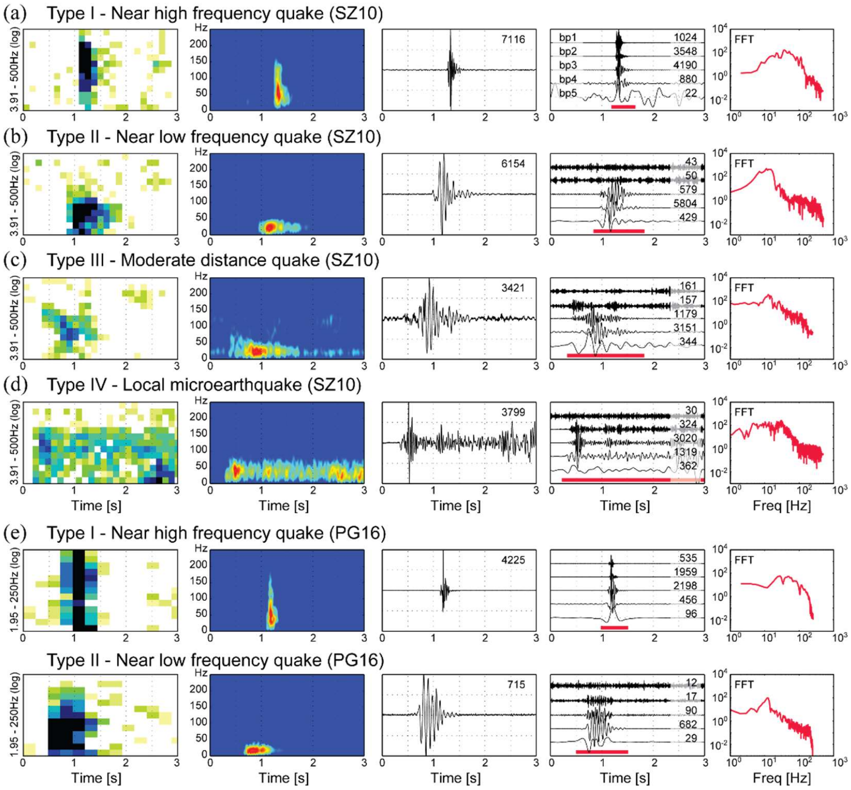

Figure 4. (a-d) Seismic features of the highest SNR/amplitude trace of events presented in Figure 2 and corresponding to type I-type IV quakes. (a) Type I, SZ10, S1.4, t_0 2010.05.29 23:05:04. (b) Type II, SZ10, S1.2, t_0 2010.06.26 18:44:55. (c) Type III, SZ10, S3.0, t_0 2010.06.17 15:32:45.500. (d) Type IV, SZ10, S2.1, t_0 2010.06.17 11:24:29.300. (e) Example of near quakes recorded at Pechgraben. Top: Type I, PG16, S2.6, t_0 2016.11.07 22:43:05.500. Bottom: Type II, PG16, S1.4, t_0 2016.11.09 01:50:13.

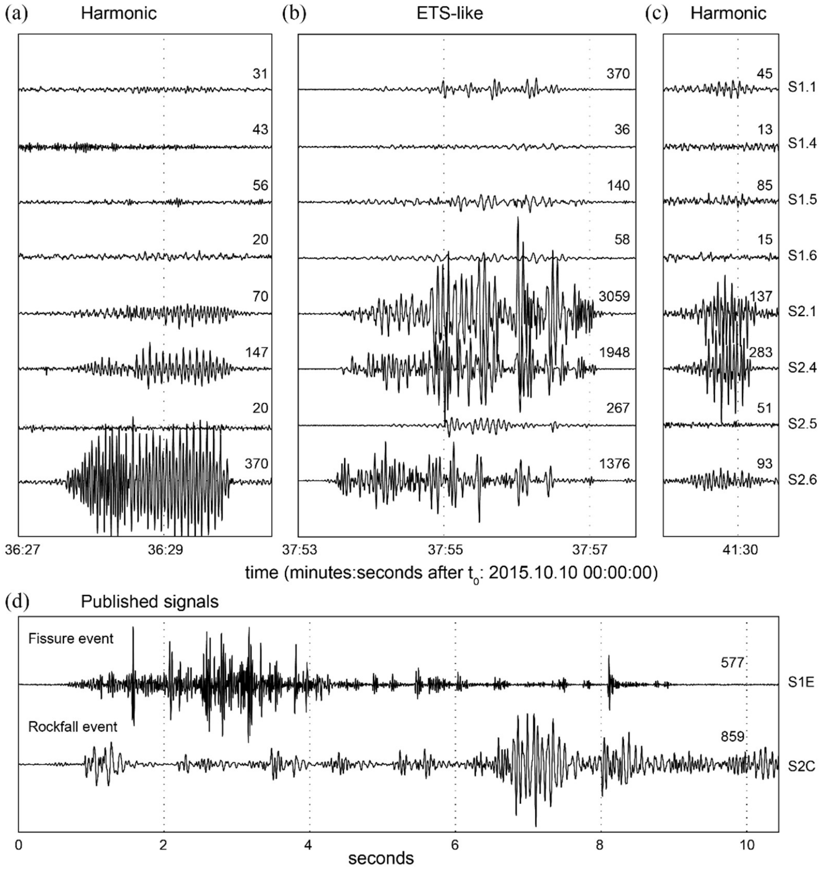

Figure 5. (a-c) Vertical trace seismograms featuring selected signals of a 40 minutes long tremor sequence recorded October 10, 2015 between 00:35 and 01:15 at PG15. See station nomenclature in Figure 1. Waveforms are normalized to the highest amplitude trace of individual events and maximum 0-to-peak amplitudes are given in nm s^{-1} on top of each seismogram. Event (a) and (c) are harmonic tremors, event (b) corresponds to an ETS-like event. Note the prominent attenuation of the waveforms and the relatively lower amplitudes of harmonic tremors. (d) Signals published in Walter et al. (2012) and interpreted as a fissure event (top, t_0 2008.07.14 23:48:40) and a rockfall event (bottom, t_0 2008.07.14 23:49:04). For better comparison, waveforms are plotted using the same time scale as in a-c.

(a) ETS-like

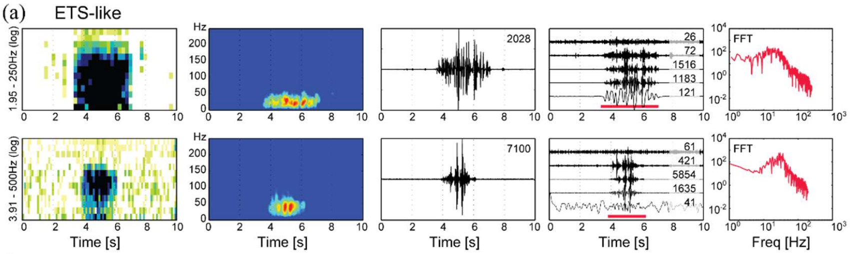

(b) Confirmed rockfall

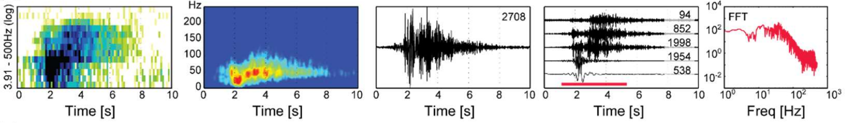

(c) Harmonic

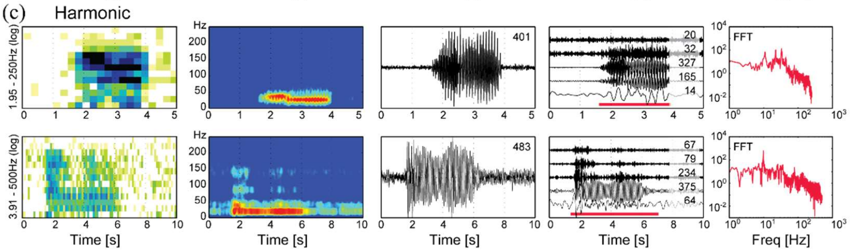

(d) Published signals

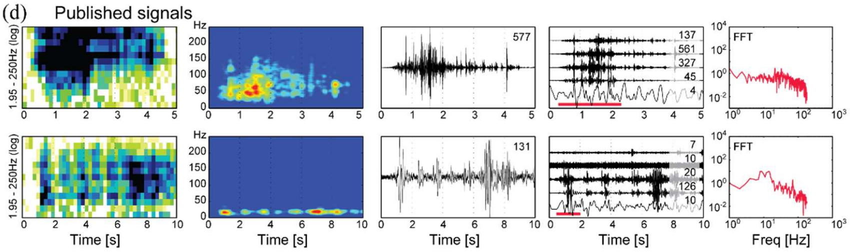

Figure 6. Seismic features of moderate duration (< 20 s) tremor signals recorded at Super-Sauze and Pechgraben. (a) ETS-like events. Top: PG15, S2.4, t_0 2015.10.10 00:37:50. Bottom: SZ10, S3.4, t_0 2010.06.05 15:26:35. (b) Confirmed rockfall event (Rothmund et al., 2017), SZ10, S2.5, t_0 2010.06.04 06:45:20. (c) Harmonic tremors. Top: PG15, S2.6, t_0 2015.10.10 00:36:26. Bottom: SZ10, S2.3, t_0 2010.06.04 20:07:28. (d) Published tremor signals by Walter et al. (2012). Top: Fissure event, t_0 2008.07.14 23:48:40. Bottom: Rockfall event, t_0 2008.07.14 23:49:04.

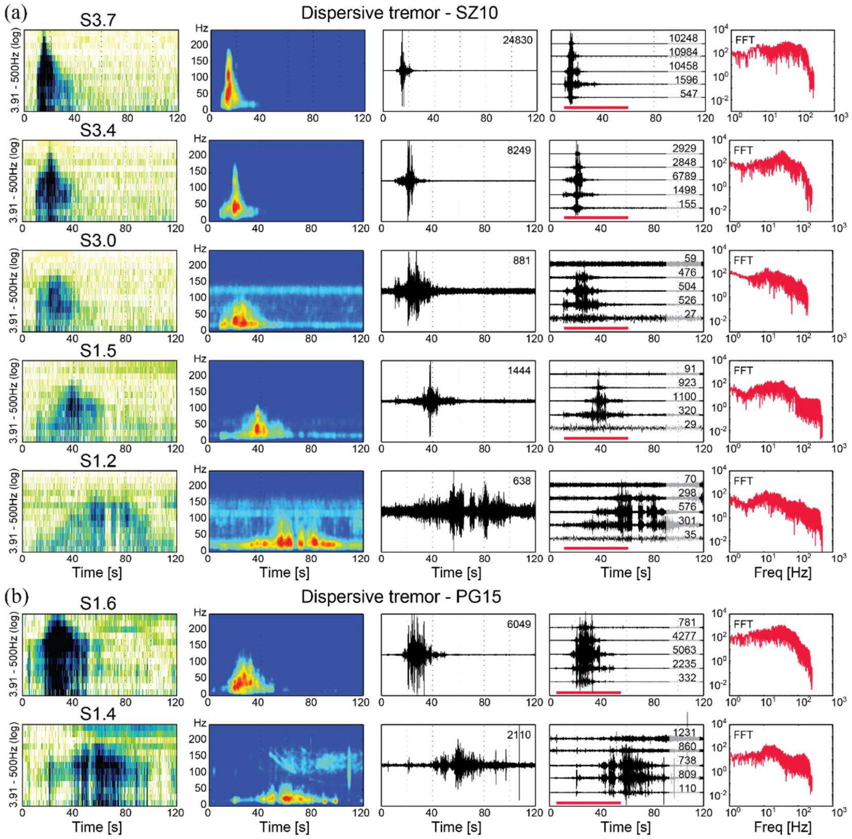

Figure 7. Seismic features of two dispersive tremor events recorded at (a) SZ10 at t₀ 2010.07.04 00:45:20 and (b) PG15 at t₀ 2015.10.08 18:02:08. Stations are indicated on top of the sonogram panels and displayed in (a) and (b) from top to bottom with increasing distance to the source (SZ10 stations S3.7 and S1.2 are about 120 m distant; PG15 stations S1.6 and S1.4 are about 50 m distant). Note the noise contamination by an airplane (gliding harmonics in the spectrogram) well visible at PG15 station S1.4. The airplane signal was well recorded by the complete seismic network, whereas the dispersive event is only seen at array S1 stations.

(a) Human footsteps

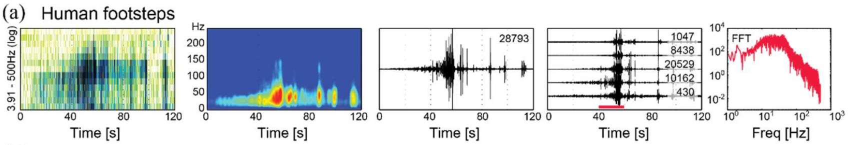

(b) Airplane

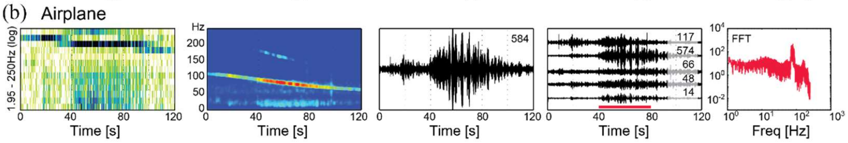

(c) Environmental noise (SZ10)

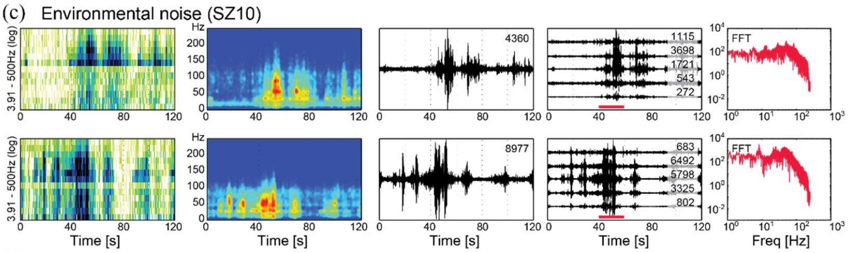

(d) Environmental noise (PG16)

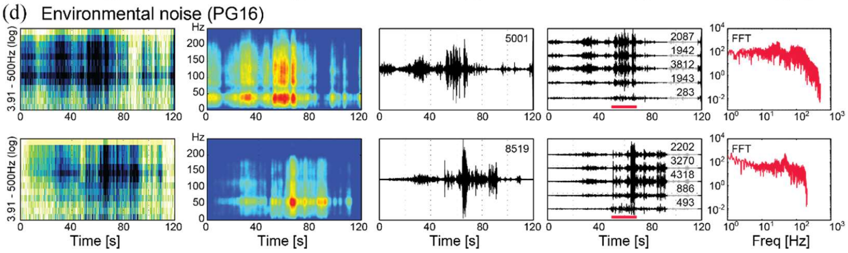

Figure 8. Seismic features of external sources (non-exhaustive) of tremor-like radiations. (a) Human footsteps at SZ10, S1.2, t_0 2010.06.05 13:08:33. (b) Airplane at PG16, S2.1, t_0 2016.11.08 04:56:00 with typical gliding harmonics in the spectrogram. (c) Environmental noise recorded at SZ10, stations S2.3 (top) and S3.8 (bottom) at t_0 2010.06.09 22:54:10 and (d) at PG16, stations S2.1 (top) and S3.1 (bottom) at t_0 2016.11.08 03:00:40.

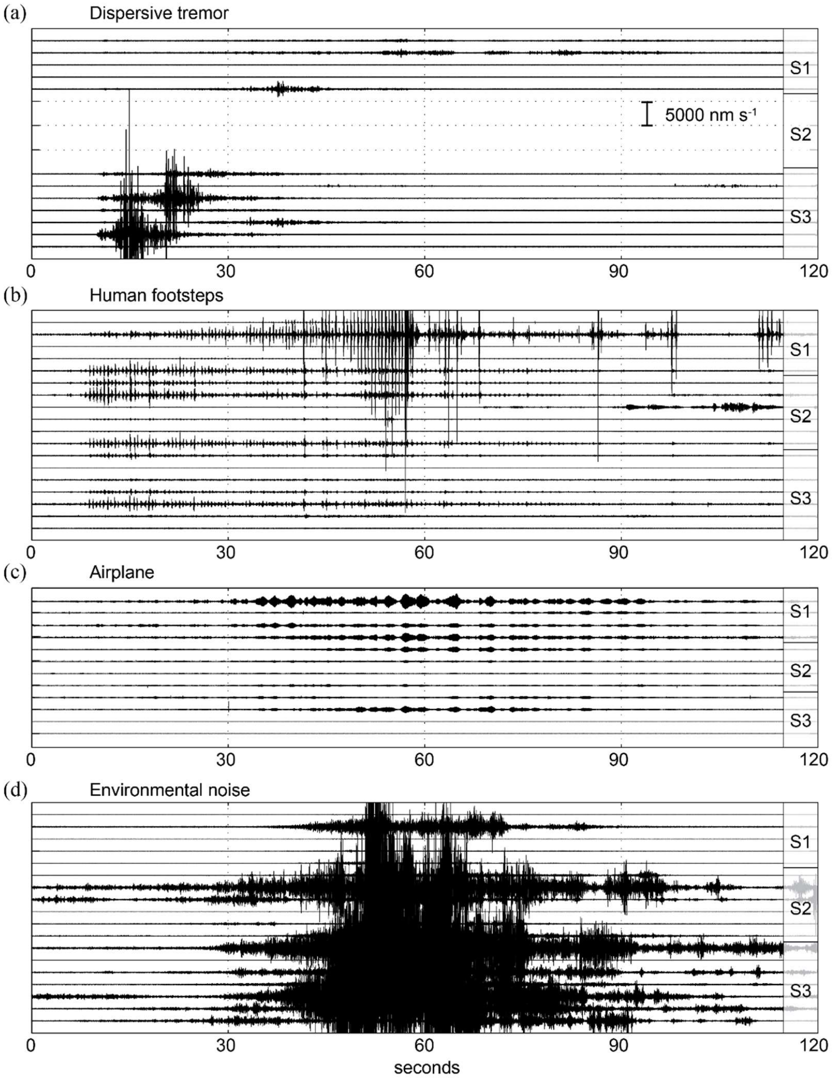

Figure 9. Vertical trace seismograms of long duration tremor-like signals recorded at Super-Sauze and Pechgraben. A constant time and amplitude scale (indicated in (a)) is applied. (a) Dispersive tremor, SZ10, t_0 2010.07.04 00:45:20. (b) Human footsteps, SZ10, t_0 2010.06.05 13:08:33. (c) Airplane, PG16, t_0 2016.11.08 04:56:00. (d) Environmental noise, SZ10, t_0 2010.06.09 22:54:10.

5

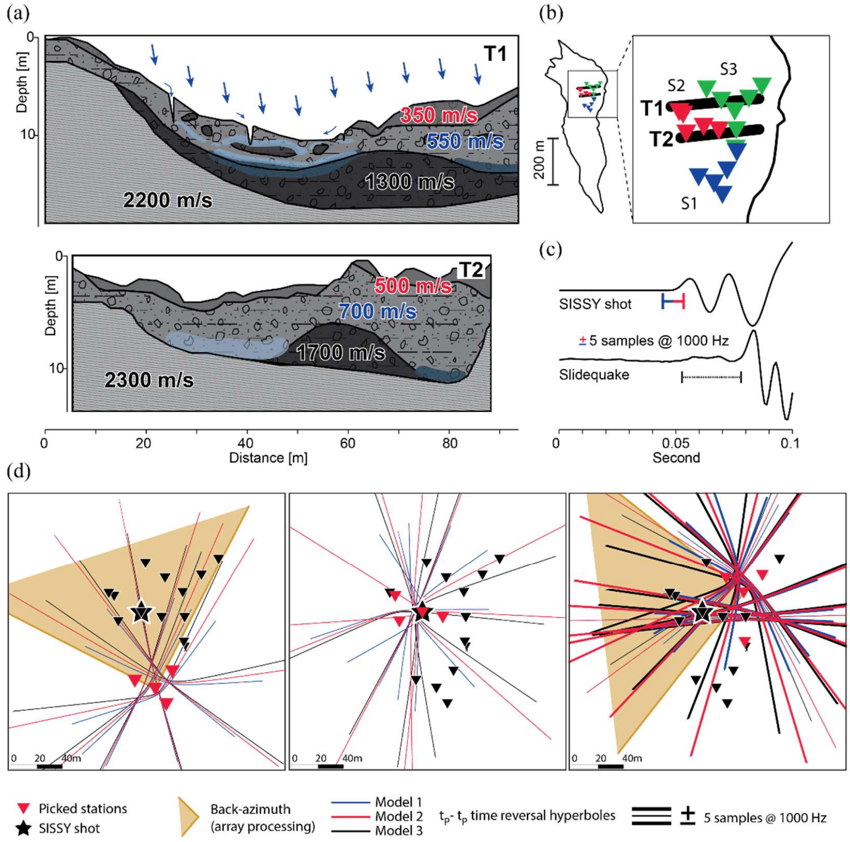

Figure 10. Parameters impacting location uncertainties at clayey landslides. (a) Complex seismic velocity structures along two tomographic profiles T1 and T2 at Super-Sauze; modified from Tonnellier et al. (2013) and Gance et al. (2016). (b) Location of the tomographic profiles T1 and T2 within the seismic arrays S1, S2, S3. (c) High-quality first arrival of a SISSY calibration shot (top trace, SZ10, S2.2, t_0 2010.06.04 11:56:22) and first arrival of a high-SNR quake type I event (bottom trace, SZ10, 2010.05.29 23:05:03). Note the higher uncertainties about the onset of the natural event. (d) Graphical location solutions for the SZ10 SISSY calibration shot at station S2.1, June 4, 2010, 11:56:22 derived from first arrivals at individual seismic array S1 (left panel), S2 (middle panel) and S3 inner ring (right panel). Picked stations are indicated by red triangles, beam-processing results are symbolized by shaded orange quadrants, time-reversal hyperboles derived with three different velocity models (Table 2) are represented by blue, red and black colored lines. In the right panel, bold hyperboles image the effect of ± five samples uncertainties shifts in first arrivals. Discussion is found in Section 5.1.

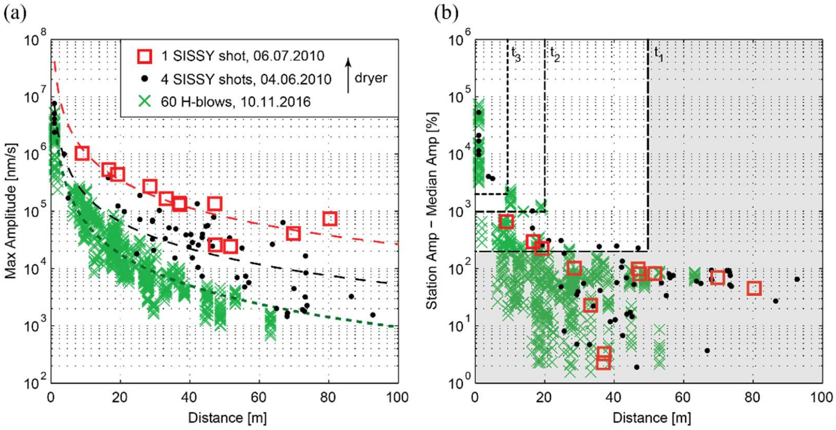

Figure 11. (a) Maximum 0-to-peak amplitudes with distance to the source of SISSY calibration shots carried out at Super-Sauze June 4 (dots) and July 6 (squares), 2010, and hammer blows (crosses) carried out at Pechgraben, November 10, 2016. Dotted lines indicate log-log regression curves. Note the lower attenuation with dryer conditions. (b) Scatter about the median amplitude of the calibration datasets presented in (a). Scatter about the median amplitude values of natural events higher than 200, 1000 and 2000 % are inferred to image receiver-source distances of about 50, 20 and 10 m (t_1 t_2 t_3) respectively. 5

Earth Surf. Dynam. Discuss., https://doi.org/10.5194/esurf-2017-65
Manuscript under review for journal Earth Surf. Dynam.
Discussion started: 23 November 2017

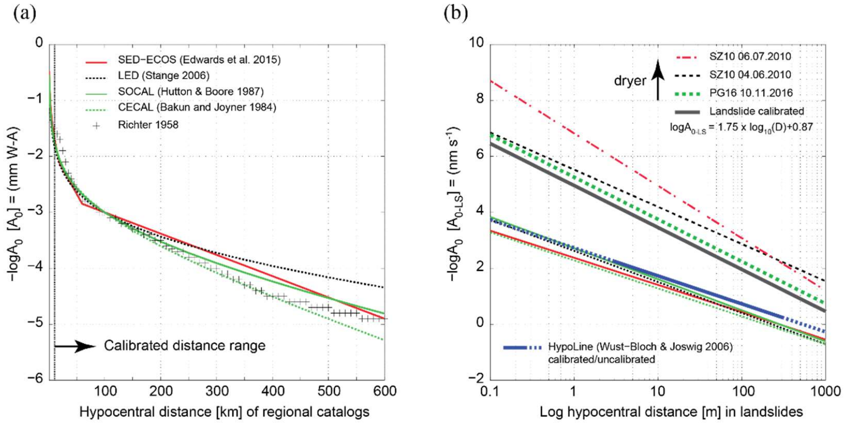

Figure 12. (a) Distance attenuation functions (-log(A_0)) of regional M_L scales empirically calibrated for receiver-source distances between 10 and 600-1000 km. (b) Log-log zoom into the valid receiver-source distance range of landslide-induced seismic signals. The HypoLine distance attenuation function, which was calibrated between 3 and 300 m in the Dead Sea Valley (Wust-Bloch and Joswig, 2006) is very similar to the projection of the regional M_L scales. The distance attenuation regression curves derived from SISSY calibration shots and hammer blows data (see Figure 11) project in the upper area of the graphic, all with steeper slopes (imaging stronger attenuation) than the regional M_L scales. The landslide calibrated distance attenuation function applies an average slope of 1.75 with an intercept of 0.87. Note that regional M_L scales use displacement amplitudes in WA mm, whereas $M_{L\text{-}LS}$ scale is calibrated using velocity readings in nm s^{-1}. See discussion in Section 5.3.

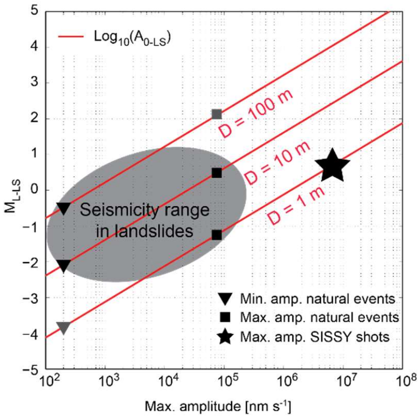

Figure 13. $M_{L\text{-}LS}$ as a function of amplitude read in 1, 10 and 100 m receiver-source distances. The star indicates the average maximum amplitude reads of SISSY calibration shots in 1 m distance that corresponds to a $M_{L\text{-}LS}$ 0.58. Minimum and maximum signal amplitudes observed for landslide-induced signals are symbolized by triangles and squares respectively. Grey symbols indicate lower probability valid distances of low and high amplitude values. A reasonable field of potential M_L of landslide-induced events is outlined by the shaded ellipse.

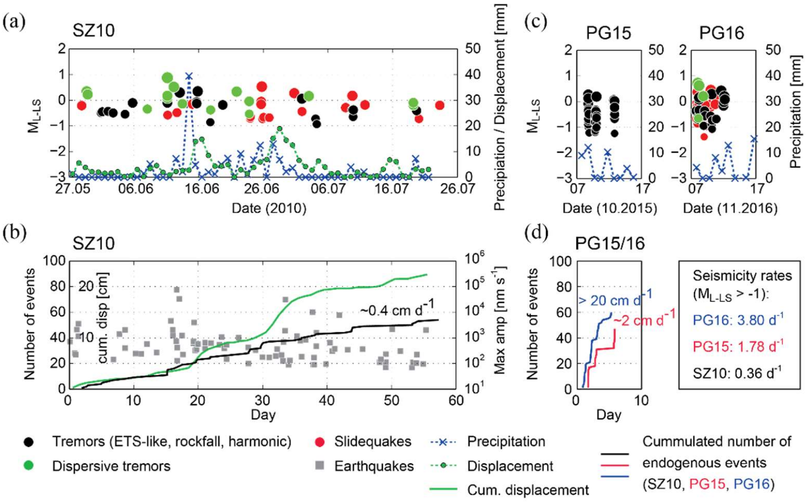

Figure 14. (a) Temporal distribution of $M_{L\text{-}LS}$ for near (< 50 m) landslide-induced events at SZ10 with displacement and precipitation data. (b) Cumulative number of landslide-induced events and cumulative displacement at SZ10 with the energy radiated by local and regional earthquakes (events median maximum 0-to-peak amplitudes in nm s^{-1}). (c) Temporal distribution of $M_{L\text{-}LS}$ for near (< 50 m) landslide-induced events at PG15 and PG16 with precipitation data. (d) Cumulative number of landslide-induced seismic events at PG15 and PG16. Seismicity rates ($M_{L\text{-}LS}$ > -1) show a clear increase with higher average displacement rates.

References

Bakun, W. H. and Joyner, W. B.: The ML scale in Central California, Bulletin of the Seismological Society of America, 74, 1827–1843, 1984.

Beard, F. D.: Predicting slides in cut slopes, Western Construction, San Fransisco, 36, 72, 1961.

Brückl, E., Brunner, F. K., Lang, E., Mertl, S., Müller, M., and Stary, U.: The Gradenbach Observatory—monitoring deep-seated gravitational slope deformation by geodetic, hydrological, and seismological methods, Landslides, 10, 815–829, doi:10.1007/s10346-013-0417-1, 2013.

Brückl, E. and Mertl, S.: Seismic monitoring of deep-seated mass movements, Disaster Mitigation of Debris Flows, Slope Failures and Landslides, Universal Academy Press, Inc. Tokyo, Japan, 571–580, 2006.

Cadman, J. D. and Goodman, R. E.: Landslide noise, Science, 158, 1182–1184, doi:10.1126/science.158.3805.1182, 1967.

Chouet, B.: Resonance of a Fluid-Driven Crack: Radiation Properties and Implications for the Source of Long-Period Events and Harmonic Tremor, Journal of Geophysical Research, 93, 4375–4400, 1988.

Deichmann, N.: Theoretical Basis for the Observed Break in ML / Mw Scaling between Small and Large Earthquakes, Bulletin of the Seismological Society of America, 107, 505–520, doi:10.1785/0120160318, 2017.

Diehl, T., Kissling, E., Husen, S., and Aldersons, F.: Consistent phase picking for regional tomography models: application to the greater Alpine region, Geophysical Journal International, 176, 542–554, doi:10.1111/j.1365-246X.2008.03985.x, 2009.

Eberhardt, E., Spillmann, T., Maurer, H., Willenberg, H., Loew, S., and Stead, D.: The Randa Rockslide Laboratory: Establishing brittle and ductile instability mechanisms using numerical modelling and microseismicity, 9th International Symposium of Landslides, Rio de Janeiro, A. A. Balkema, Leiden, 481–487, 2004.

Edwards, B., Kraft, T., Cauzzi, C., Kastli, P., and Wiemer, S.: Seismic monitoring and analysis of deep geothermal projects in St Gallen and Basel, Switzerland, Geophysical Journal International, 201, 1022–1039, doi:10.1093/gji/ggv059, 2015.

Fischer, T., Roth, M., and Kühn, D.: Seismic monitoring of a rock slope Åknes, Norway: time-reversal localization of seismic activity, Geophysical Research Abstracts, 16, 2014.

Gance, J., Malet, J.-P., Supper, R., Sailhac, P., Ottowitz, D., and Jochum, B.: Permanent electrical resistivity measurements for monitoring water circulation in clayey landslides, Journal of Applied Geophysics, 126, 98–115, doi:10.1016/j.jappgeo.2016.01.011, 2016.

Gomberg, J., Bodin, P., Savage, W., and Jackson, M. E.: Landslide faults and tectonic faults, analog?: The Slumgullion earthflow, Colorado, Geology, 23, 41–44, 1995.

Gomberg, J., Schulz, W., Bodin, P., and Kean, J.: Seismic and geodetic signatures of fault slip at the Slumgullion Landslide Natural Laboratory, Journal of Geophysical Research, 116, doi:10.1029/2011JB008304, 2011.

Helmstetter, A. and Garambois, S.: Seismic monitoring of Séchilienne rockslide (French Alps): Analysis of seismic signals and their correlation with rainfalls, J. Geophys. Res., 115, doi:10.1029/2009JF001532, 2010.

Helmstetter, A., Moreau, L., Nicolas, B., Comon, P., and Gay, M.: Intermediate-depth icequakes and harmonic tremor in an Alpine glacier (Glacier d'Argentière, France): Evidence for hydraulic fracturing?, J. Geophys. Res. Earth Surf., 120, 402–416, doi:10.1002/2014JF003289, 2015.

Hungr, O., Leroueil, S., and Picarelli, L.: The Varnes classification of landslide types, an update, Landslides, 11, 167–194, doi:10.1007/s10346-013-0436-y, 2014.

Hutton, L. K. and Boore, D. M.: The ML scale in southern California, Bulletin of the Seismological Society of America, 77, 2074–2094, 1987.

Joswig, M.: Pattern recognition for earthquake detection, Bulletin of the Seismological Society of America, 80, 170–186, 1990.

Joswig, M.: Nanoseismic monitoring fills the gap between microseismic networks and passive seismic, special topic, Leveraging Technology, first break, 26, 117–124, 2008.

Jurich, D. M. and Miller Russell J.: Acoustic monitoring of landslides, Geotechnology, Transportation Research Record, 30–38, 1987.

Koerner, R. M., McCabe, W. M. and Lord, A. E.: Acoustic emission behavior and monitoring of soils, Acoustic emissions in geotechnical engineering practice, ASTM International, 93-141, doi: 10.1520/STP28343S, 1981.

Lacroix, P. and Helmstetter, A.: Location of Seismic Signals Associated with Microearthquakes and Rockfalls on the Sechilienne Landslide, French Alps, Bulletin of the Seismological Society of America, 101, 341–353, doi:10.1785/0120100110, 2011.

Lipovsky, B. P. and Dunham, E. M.: Tremor during ice-stream stick slip, The Cryosphere, 10, 385–399, doi:10.5194/tc-10-385-2016, 2016.

Malet, J.-P.: Les glissements de type écoulement dans les marnes noires des Alpes du Sud. Morphologie, fonctionnement et modélisation hydro-mécanique. Thèse de Doctorat, Université Louis Pasteur, Strasbourg, France 364 p.

Malet, J.-P., Laigle, D., Remaître, A., and Maquaire, O.: Triggering conditions and mobility of debris flows associated to complex earthflows, Geomorphology, 66, 215–235, doi:10.1016/j.geomorph.2004.09.014, 2005.

Mertl, S. and Brückl, E.: Observation of fracture processes in creeping rock masses by seismic monitoring, in: Proceedings of 11th Congress of the ISRM, Lisbon, Portugal, 9-13 July 2007, 2007.

National French Landslide Observatory Facility and RESIF Datacenter: French Multidisciplinary Observatory of Versant Instabilities, Université de Grenoble Alpes, 2006.

Provost, F., Hibert, C., and Malet, J.-P.: Automatic classification of endogenous landslide seismicity using the Random Forest supervised classifier, Geophys. Res. Lett., 44, 113–120, doi:10.1002/2016GL070709, 2017.

Richter, C. F.: Elementary Seismology, W.H. Freeman and Co., San Fransisco, 1958.

Roth, M., Dietrich, M., Blikra, L. H., and Lecomte, I.: Seismic monitoring of the unstable rock slope site at Aknes, Norway, NORSAR Report, Oslo, 2005.

Rothmund, S., Vouillamoz, N., and Joswig, M.: Mapping slow-moving alpine landslides by UAV — Opportunities and limitations, The Leading Edge, 36, 571–579, doi:10.1190/tle36070571.1, 2017.

Schlindwein, V., Wassermann, J., and Scherbaum, F.: Spectral analysis of harmonic tremor signals at Mt. Semeru volcano, Indonesia, Geophys. Res. Lett., 22(13), 1685-1688, 1995.

Sick, B., Walter, M., and Joswig, M.: Visual Event Screening of Continuous Seismic Data by Supersonograms, Pure and Applied Geophysics, doi:10.1007/s00024-012-0618-x, 2012.

Spillmann, T., Maurer, H., Green, A. G., Heincke, B., Willenberg, H., and Husen, S.: Microseismic investigation of an unstable mountain slope in the Swiss Alps, Journal of Geophysical Research, 112, doi:10.1029/2006JB004723, 2007.

Stange, S.: ML Determination for Local and Regional Events Using a Sparse Network in Southwestern Germany, Journal of Seismology, 10, 247–257, doi:10.1007/s10950-006-9010-6, 2006.

Tonnellier, A., Helmstetter, A., Malet, J.-P., Schmittbuhl, J., Corsini, A., and Joswig, M.: Seismic monitoring of soft-rock landslides: the Super-Sauze and Valoria case studies, Geophysical Journal International, 193, 1515–1536, doi:10.1093/gji/ggt039, 2013.

Travelletti, J.: Travelletti, J. 2011. Imagerie multi-paramètres et multi-résolutions pour l’observation et la caractérisation des mécanismes de glissements-coulées. Thèse de Doctorat, Université de Strasbourg, France 318p.

Vouillamoz, N., Wust-Bloch, G. H., Abednego, M., and Mosar, J.: Optimizing Event Detection and Location in Low-Seismicity Zones: Case Study from Western Switzerland, Bulletin of the Seismological Society of America, 106, 2023–2036, doi:10.1785/0120160029, 2016.

Walter, M., Arnhardt, C., and Joswig, M.: Seismic monitoring of rockfalls, slide quakes, and fissure development at the Super-Sauze mudslide, French Alps, Engineering Geology, 128, 12–22, doi:10.1016/j.enggeo.2011.11.002, 2012.

Walter, M. and Joswig, M.: Seismic monitoring of fracture processes generated by a creeping landslide in the Vorarlberg Alps, first break, 26, 131–135, 2008.

Walter, M. and Joswig, M.: Seismic characterization of slope dynamics caused by softrock-landslides: the Super-Sauze case-study, in: Proceedings of the International Conference on Landslide Processes: from geomorphologic mapping to dynamic modelling, Malet, J.-P., Remaître, A., and Boogard, T. A. (Eds.), CERG Editions, Strasbourg, 215–220, 2009.

Walter, M., Walser, M., and Joswig, M.: Mapping Rainfall-Triggered Slidequeakes and Seismic Landslide-Volume Estimation at Heumoes slope, Vadose Zone Journal, 10, 487–495, 2011.

Williams, R. A. and Pratt, T. L.: Detection of the base Slumgullion landslide, Colorado, by seismic reflection and refraction methods, in: The Slumgullion Earth Flow: A Large-Scale Natural Laboratory, Varnes, D. J., and Savage, W. Z. (Eds.), U.S. Geol. Surv. Bull., 2130, 77–84, 1996.

Wust-Bloch, G. H. and Joswig, M.: Pre-collapse identification of sinkholes in unconsolidated media at Dead Sea area by ‘nanoseismic monitoring’ (graphical jackknife location of weak sources by few, low-SNR records), Geophysical Journal International, 167, 1220–1232, doi:10.1111/j.1365-246X.2006.03083.x, 2006.